

# Optimising Microwave Cavities for nonzero Helicity with Machine Learning

Emma Paterson,<sup>1</sup> Jeremy Bourhill,<sup>1</sup> and Maxim Goryachev<sup>1,\*</sup>

<sup>1</sup>*Quantum Technologies and Dark Matter Labs, Department of Physics, University of Western Australia, Crawley, Perth 6009, Australia*

(Dated: February 11, 2026)

We present a machine-learning-driven inverse design framework for systematically engineering three-dimensional microwave cavity resonators that support modes with nonzero electromagnetic helicity. In contrast to heuristic approaches to cavity design, helicity maximisation is formulated as a boundary-shape optimisation problem, enabling systematic exploration of complex boundary-shape parameter spaces and the identification of high-helicity designs that are difficult to predict using heuristic design rules alone. We applied this framework to several cavity families composed of smooth, edge-free components, including globally twisted cavities with control-point-defined cross-sections realised in both linear and ring configurations, cavities defined by the intersection of orthogonal prisms, sphere-subtracted cylindrical cavities, and parametrised surface resonators. Two gradient-free optimisation strategies, a genetic algorithm and Bayesian optimisation, were independently employed to explore compact sets of design parameters for these geometries and to optimise a scaled-helicity figure of merit for the dominant helical mode, evaluated via finite-element eigenmode analysis. Robustness to manufacturing tolerances was quantified by applying Gaussian geometric perturbations to the optimised cavities and evaluating statistical robustness metrics that penalise sensitivity to geometric variation.

## INTRODUCTION

Over the past decade, inverse design methodologies, originally developed for nanophotonic devices, have transformed how electromagnetic structures are conceived, moving from intuition-driven layouts to algorithmically discovered geometries that maximize performance metrics with minimal human intervention. At their core, these methods couple a flexible parameterisation of device geometry (e.g. pixel-level permittivity maps or level-set boundaries) with a rigorous electromagnetic solver and an optimisation engine [1–3].

In a typical adjoint-based workflow, a forward simulation evaluates a figure-of-merit (FoM), such as quality factor, mode volume, or bandwidth, then a single adjoint solve yields gradients of the FoM with respect to every design parameter, enabling efficient updates even when millions of degrees of freedom are involved. When gradients are unreliable or the design must satisfy discrete constraints (e.g. minimum feature sizes, binary materials), gradient-free alternatives like genetic algorithms (GA) or Bayesian optimisation (BO) can guide the search.

Inverse design has already reshaped applications across the spectrum of electromagnetics: ultracompact wavelength demultiplexers [2, 4], beam-steering metasurfaces [5] and photonic-crystal circuits [6], ultra-broadband power splitters [2] and directional couplers [2] in photonics; broadband filters, resonant RF structures, power splitters, combiners, diplexers, and antennas in the radio-frequency domain [7]; and even chiral metamaterials engineered for strong optical activity [8]. In each case, the automated routine often uncovers non-intuitive

geometries, complex mode converters [6], or aperiodic perforation patterns [3, 9] that outperform conventional hand-designed counterparts in footprint, loss, or functional versatility.

In this work, we apply inverse-design principles to iteratively refine the metallic boundaries of three-dimensional (3D) microwave cavities. The optimisation is driven by a FoM based on electromagnetic helicity,  $\mathcal{H}$ , defined as the projection of the electromagnetic spin onto its momentum [10–13]. This approach enables the discovery of cavity resonators that support highly helical electromagnetic modes.

For a monochromatic resonant mode  $i$ , the local helicity density,  $h(\vec{r})$ , is defined as [14]

$$h_i(\vec{r}) = 2 \operatorname{Im} \left[ \vec{\mathbf{e}}_i(\vec{r}) \cdot \vec{\mathbf{h}}_i^*(\vec{r}) \right] = \frac{2 \operatorname{Im} \left[ \vec{\mathbf{E}}_i(\vec{r}) \cdot \vec{\mathbf{H}}_i^*(\vec{r}) \right]}{V \mathcal{E} \mathcal{H}}, \quad (1)$$

where  $V$  is the cavity volume;  $\vec{\mathbf{E}}_i(\vec{r}) = \mathcal{E} \vec{\mathbf{e}}_i(\vec{r})$  and  $\vec{\mathbf{H}}_i(\vec{r}) = \mathcal{H} \vec{\mathbf{h}}_i(\vec{r})$  are the electric and magnetic vector fields, with  $\mathcal{E}$  and  $\mathcal{H}$  being real constants; and the normalised position dependent eigenvectors,  $\vec{\mathbf{e}}_i(\vec{r})$  and  $\vec{\mathbf{h}}_i(\vec{r})$ , satisfy  $\frac{1}{V} \int |\vec{\mathbf{e}}_i(\vec{r})|^2 dV = \frac{1}{V} \int |\vec{\mathbf{h}}_i(\vec{r})|^2 dV = 1$ . Physically, generating large  $h_i(\vec{r})$  means that the fields exhibit a well-defined handedness, creating regions with significant spatial overlap between parallel components of  $\vec{\mathbf{E}}_i$  and  $\vec{\mathbf{H}}_i$ . The total helicity is then defined as

$$\mathcal{H}_i = \int h_i(\vec{r}) dV, \quad (2)$$

providing a quantitative measure of the global chirality of the electromagnetic mode.

The quantity  $\mathcal{H}_i$  is dimensionless because  $h_i(\vec{r})$  is normalised by the total electromagnetic amplitudes of the resonant mode, a choice reflected in the factor of two

\* maxim.goryachev@uwa.edu.au

in (1). By the Cauchy-Schwarz inequality,  $|\mathcal{H}_i/2| \leq 1$ , implying that  $|\mathcal{H}_i| \leq 2$ , with the limiting values  $\mathcal{H}_i = \pm 2$  corresponding to maximally helical fields.

In our optimisation algorithm, we target the magnitude of  $\mathcal{H}_i$  rather than its sign. If an application requires the opposite handedness, the cavity can be realised as the mirror image of the optimised geometry.

Heuristically designed microwave cavity resonators engineered to support large  $|\mathcal{H}_i|$  have been reported [14–17]. These resonators consist of prisms with a  $D_n$  cross-section whose spatial symmetry is broken by introducing a uniform twist along the prism height. This symmetry breaking leads to the emergence of eigenmodes with nonzero  $|\mathcal{H}_i|$  through two primary distinct mechanisms: hybridisation of near-degenerate transverse-electric (TE) and transverse-magnetic (TM) modes, and self-interference of the modes. Irregardless of the mechanism, it's the  $\vec{\mathbf{E}}_i(\vec{r})$  and  $\vec{\mathbf{H}}_i(\vec{r})$  fields co-existing in space with some degree of non-orthogonality that defines the  $|\mathcal{H}_i|$  of the helical mode in these twisted resonators, and the composite modes of the non-twisted resonator are irrelevant.

Such heuristic approaches therefore do not provide a reliable or systematic route to optimising  $|\mathcal{H}_i|$ . This is because  $|\mathcal{H}_i|$  depends on the spatial overlap between parallel components of the  $\vec{\mathbf{E}}_i(\vec{r})$  and  $\vec{\mathbf{H}}_i(\vec{r})$  fields throughout the entire 3D cavity volume and can change sharply under small boundary perturbations. As a result, it is difficult to reliably predict what 3D boundary conditions will maximise  $|\mathcal{H}_i|$ , and the optimal geometries are often non-intuitive. This makes the optimisation problem a natural candidate for inverse design using machine-learning-based optimisation, where algorithms can efficiently explore large boundary-shape parameter spaces and uncover cavity geometries that would be unlikely to be identified using heuristic design alone.

The ability to systematically engineer cavities with large  $|\mathcal{H}_i|$  enables a broad range of applications. The resulting nonzero  $|\mathcal{H}_i|$  facilitates strong coupling to chiral matter and pseudoscalar sources, enhancing the strength of associated interactions and providing a versatile platform for both fundamental studies of chiral electrodynamics and a wide range of practical applications. These include enantioselective microwave spectroscopy, which enables discrimination between left- and right-handed molecular conformers [18, 19], enhanced circular dichroism for improved sensitivity in chiral sensing and catalytic processes [20], and parity-violation experiments in which nonzero  $h_i(\vec{r})$  amplifies weak-interaction signals in atomic and nuclear transitions. These applications further extend to axion dark-matter searches, where the axion-photon coupling term scales with the local helicity density  $h_i(\vec{r})$ , increasing conversion efficiency [21]. Additional applications include chiral quantum sensing, which enables spin-selective interactions with defect centers such as nitrogen-vacancy (NV) centers through  $\mathcal{H}$ -matched modes [22]; nonreciprocal microwave devices, including isolators and circulators that exploit broken

time- and parity-symmetries [23]; and topological microwave photonics, where  $\mathcal{H}$ -engineered modes can realise protected edge states and spin-momentum locking [24].

This paper is organised as follows. Sec. 1 outlines the principal challenges associated with applying inverse design to fully 3D microwave cavities and motivates the inverse design framework developed in this work. Sec. 2 then details this framework, describing the pipeline linking Python to finite-element simulations for evaluating the fitness of a given cavity geometry (Sec. 2.1), the optimisation strategies employed (Sec. 2.2), and the assessment framework for the optimised cavities, which defines mesh-convergence tests (Sec. 2.3) and key performance metrics (Sec. 2.4). Sec. 3 presents the results of applying this inverse-design framework to a range of cavity families composed of smooth, edge-free (EF) components, examining how variations in geometry and parameterisation influence the optimisation outcomes. These families include globally twisted linear and ring cavities (Secs. 3.1 and 3.2), orthogonal prism-intersection cavities (Sec. 3.3), sphere-subtracted cylindrical cavities (Sec. 3.4), and parameterised-surface cavities (Sec. 3.5). The results are synthesised in the Discussion, followed by a summary of the key findings and outlook in the Conclusion.

## 1. INVERSE DESIGN OF MICROWAVE CAVITIES: CHALLENGES AND OPPORTUNITIES

### 1.1. Challenges of Inverse Design in Fully 3D Cavities

While inverse design is well established in planar photonic systems [25, 26], extending these methods to fully 3D microwave cavities introduces several unique hurdles. In photonics, one typically exploits planar or quasi-two-dimensional (quasi-2D) layouts with symmetry axes, reducing the problem to 2D permittivity maps and relatively modest mesh sizes. Dimensional-reduction techniques have also been applied to helically coiled optical waveguides, where curvature and torsion induce helicity and symmetry enables reformulation of the 3D Helmholtz problem on a 2D cross-section [27]. By contrast, inverse design in truly 3D microwave cavity resonators with no exploitable symmetries requires parametrising fully 3D metal boundaries, a more complex task than assigning binary pixels in 2D.

A second challenge is the substantially greater computational cost: simulating the volumetric meshes required to model these 3D field distributions typically involves tens to hundreds of millions of degrees of freedom. Moreover, ensuring sufficient spatial resolution to resolve

$h_i(\vec{r})$  hotspots further increases the computational burden compared with photonic systems.

Despite these challenges, inverse design has been shown to enhance the chirality of fully 3D nanostructures [28]. However, applying inverse design to metallic microwave cavities introduces additional constraints: one must account for realistic metal losses, enforce minimum feature sizes along all axes, avoid unsupported thin walls or overhangs, and accurately capture curved conductive boundaries. Such requirements make machine-learning-based inverse design of fully 3D microwave cavities significantly more demanding than in 2D photonic systems.

## 1.2. Fabrication Constraints due to Additive Manufacturing

Beyond computational and modelling challenges, experimental realisation poses additional difficulties. Existing 3D cavities supporting nonzero  $h_i(\vec{r})$  typically rely on highly curved and geometrically complex structures [14–17], which are only practically realisable through metal additive manufacturing owing to the geometric freedom it provides. However, additive manufacturing introduces several drawbacks that complicate the fabrication of precise, high-performance cavities. In particular, geometric deviations in the intended design can arise from thermal distortion during layer-by-layer deposition [31], adhesion of partially melted powder [32], the stair-step effect associated with discretised layering of curved surfaces [33], localised melting and cooling cycles [31, 34, 35], and residual-stress-induced warping [35, 36]. Such geometric variations are particularly problematic for cavity designs whose electromagnetic performance is highly sensitive to small perturbations in geometry.

A second issue with additively manufactured (AM) parts is their high surface roughness [35], porosity and micropores [37–39], and surface pits [31, 40, 41], all of which degrade surface quality. Unsupported regions that create local undercuts or rough edges [31, 42] further exacerbate surface roughness and diminish the electrical performance of the cavity.

Further complicating matters, the most effective post-processing method for improving surface quality, electropolishing, performs poorly on AM components [31], particularly those with high curvature, non-smooth transitions, sharp edges, or recessed internal features such as the structures considered here. Non-uniform primary current distribution across such features leads to uneven material dissolution and under-polished regions [31, 43–45], while restricted electrolyte and cathode access in intricate geometries further exacerbates this non-uniformity [46]. Local heat and polishing-product accumulation within confined regions additionally degrades internal surface quality [31]. Moreover, high material-removal rates hinder precise dimensional control [31, 42, 47–49], increasing geometric inaccuracies in the additively manufactured part.

## 1.3. Optimisation Design and Robustness Assessment

The microwave  $Q$ -factor is highly sensitive to surface smoothness and conductivity [50], making uniformly smooth internal surfaces in additively manufactured cavities a central challenge for realizing low-loss, high- $Q$  resonators. To address these limitations, our inverse-design optimisation is carried out over 3D cavity families constructed from smooth, EF components. By ensuring that the constituent components avoid sharp features, corners, and abrupt curvature variations, the resulting cavities are compatible with additive manufacturing and suitable for electropolishing during post-processing.

We make this optimisation tractable by restricting the search to compact geometric parameterisations. For each candidate geometry, we evaluate only a small, fixed set of eigenmodes. We also tune the PyGAD optimisation parameters to minimise the total number of finite-element eigenmode solves required.

Recent reviews highlight that most inverse-design workflows optimise only nominal device performance and provide limited or no quantitative assessment of fabrication tolerance [51]. To provide such an assessment within our framework, we evaluate the performance of each optimised design under geometric perturbations, identifying cavities that retain high  $|\mathcal{H}_i|$  under parameter variations and are therefore less sensitive to dimensional deviations introduced by electropolishing and the intrinsic fabrication tolerances of metal AM parts. Our robustness-evaluation framework thereby compresses an otherwise intractable exploration of a high-dimensional tolerance space into a small set of interpretable statistics.

## 2. METHODS

Figure 1 presents a schematic overview of the inverse design framework. The diagram illustrates how Python-based optimisation routines interface with COMSOL Multiphysics® [29] to perform electromagnetic finite-element simulations of the cavity resonators. The components of this framework are described in detail below.

### 2.1. Fitness Evaluation

For each cavity family investigated, a dedicated COMSOL model file is constructed. The model comprises a fully parameterised cavity geometry defined by a set of global geometric parameters, with perfect electric conductor boundary conditions imposed on all metallic surfaces. The cavity volume is assigned free-space material properties, characterised by a relative permittivity  $\epsilon_r = 1$ , relative permeability  $\mu_r = 1$ , and electrical conductivity  $\sigma = 0$  s/m, and the electromagnetic waves,

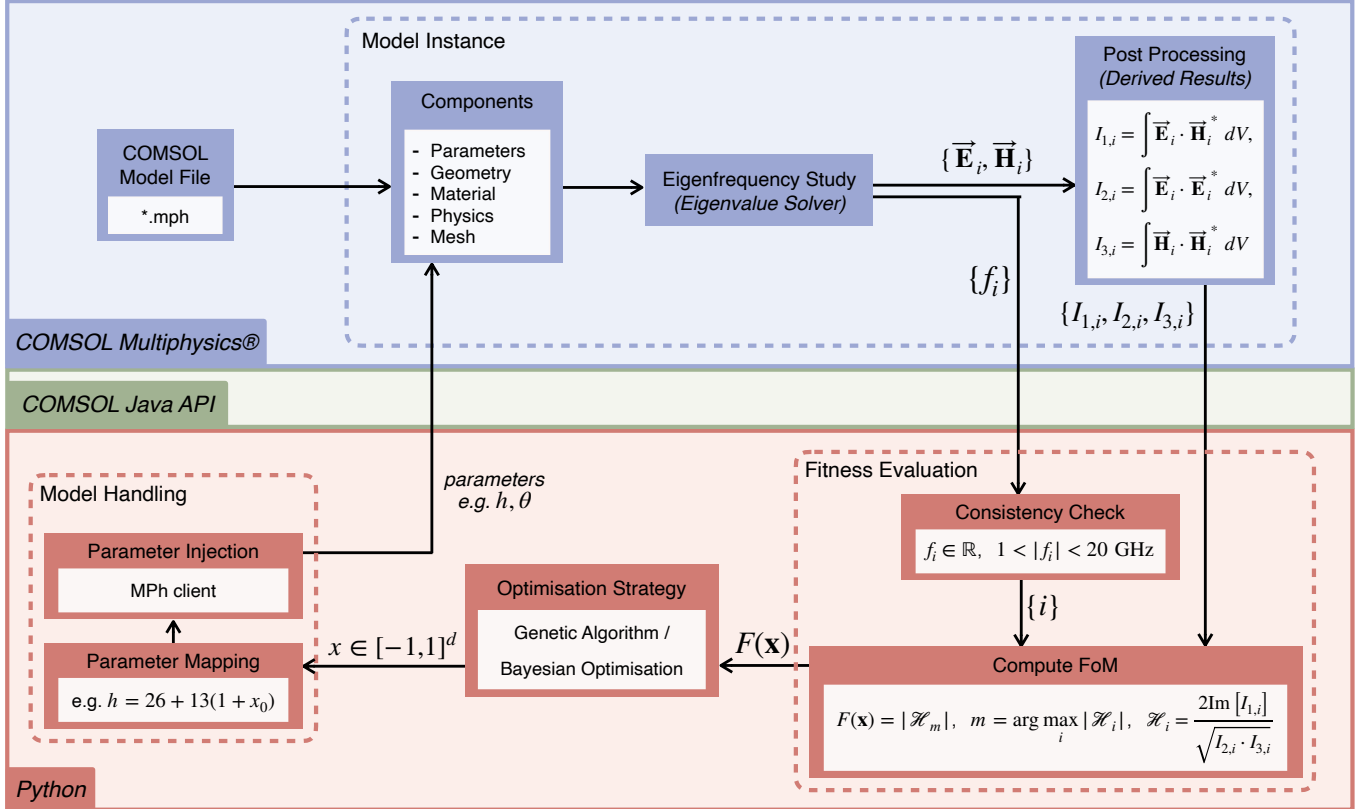


FIG. 1. Block diagram of the inverse design framework used in this work to optimise microwave cavity geometries for electromagnetic helicity,  $\mathcal{H}$ . A COMSOL Multiphysics® [29] model file containing the parameterised cavity geometry, material properties, physics interfaces, and mesh is loaded into a COMSOL model instance via an MPH [30] client using the COMSOL Java API. A normalised design vector  $\mathbf{x} \in [-1, 1]^d$ , generated by the optimisation algorithm, is mapped to physical geometric parameters and injected into the model. An eigenfrequency study is executed, yielding a set of cavity eigenmodes  $\{i\}$ , where  $i$  indexes individual eigenmodes, with corresponding eigenfrequencies  $\{f_i\}$  and  $k$  number of post-processing volume integrals  $\{I_{k,i}\}$ . For eigenmodes with real  $f_i \in [1, 20]$  GHz, the FoM  $F(\mathbf{x}) = |\mathcal{H}_m|$ , where  $m$  denotes the most helical mode in the retained set, is computed and returned to the optimisation routine, closing the optimisation loop.

frequency-domain physics interface is employed. A free tetrahedral mesh is employed to resolve the full 3D field structure, together with a predefined but unsolved eigenfrequency study and post-processing volume integrals required to evaluate  $|\mathcal{H}_i|$ .

Programmatic control of the COMSOL models is achieved using the Python package MPH [30], which provides an interface to the COMSOL Model Java API. Through MPH, a client is instantiated that launches a COMSOL session and loads the pre-defined model file. For each candidate geometry, the optimisation routine generates a normalised design vector  $\mathbf{x} \in [-1, 1]^d$ , where  $d$  is the number of geometric parameters being optimised. These parameters are affinely mapped to the corresponding physical COMSOL parameters, such as cavity height, twist angle, or radial control points, according to the specific cavity family under consideration. The admissible ranges of the physical parameters are chosen to respect fabrication constraints, ensuring that all optimised geometries are manufacturable. Expressing the design variables in terms of  $\mathbf{x}$  yields a compact, dimensionless search

space that is well suited to optimisation.

The mapped parameters are injected into the COMSOL model via the Java API, and an eigenfrequency study is executed to compute the cavity eigenmodes; the number of eigenmodes solved for is chosen on a per-geometry basis to ensure adequate sampling of the spectrum while maintaining reasonable solve times. Using this API, eigenfrequencies and post-processed volume integrals are extracted. Only modes with real eigenfrequencies in the range  $f_i \in [1, 20]$  GHz are retained; all others are discarded. The FoM for this cavity design is then computed as

$$F(\mathbf{x}) = |\mathcal{H}_m|, \quad (3)$$

where  $m$  denotes the most helical mode among the retained eigenmodes for that geometry.  $F(\mathbf{x})$  serves as the fitness value used by the optimisation algorithm.

TABLE 1. Genetic-algorithm parameters used for the optimisation of the cavity geometries.

Geometry	$N_{gen}$	$N_{par}$	$N_{pop}$	$N_{elite}$	$d$	$f_{mut}$	$\sigma_{mut}$	$\mathcal{T}_{stop}$
EF twisted linear (baseline) [Sec. 3.1]	99	9	44	10	10	0.10	0.18	saturate_98, saturate_7
EF twisted linear (expanded $r_i$ )	200	56	140	6	10	0.35	0.18	saturate_40
EF twisted ring [Sec. 3.2]	260	56	140	6	10	0.35	0.08	saturate_40
Orthogonal prism-intersection [Sec. 3.3]	123	9	47	10	16	0.10	0.18	reach_98, saturate_19
Sphere-subtracted cylindrical [Sec. 3.4]	199	11	49	10	26	0.10	0.08	reach_98, saturate_7
Parametrised surface [Sec. 3.5]	100	11	30	6	6	0.17	0.08	reach_98, saturate_7

## 2.2. Optimisation Strategies

### 2.2.1. Genetic Algorithm

A genetic algorithm (GA) is one of the optimisation strategies employed to maximise the FoM. This population-based evolutionary algorithm iteratively refines the geometry parameters through a process of selection, crossover, and mutation. At each generation, a new population of candidate geometries is generated, evaluated, and ranked according to  $F(\mathbf{x})$ . This process continues until convergence is reached, yielding a cavity shape that maximises the  $\mathcal{H}$ -based FoM.

The GA is implemented using the PyGAD library [52] with tournament selection, elitism, and Gaussian mutation. A single-point crossover is applied to combine parent solutions, while Gaussian mutation with a standard deviation of  $\sigma_{mut} = 0.08\text{--}0.18$  (depending on the cavity family) perturbs 10% of the genes in each generation. Mutations are clipped to  $[-1, 1]$  in the normalised parameter space to ensure that all design variables remain within their physical bounds. Non-convergent COMSOL simulations are penalised with a large negative fitness value to prevent invalid solutions from propagating through the population.

Key GA parameters for all optimised cavities are listed in Table 1. The population size ( $N_{pop}$ ), number of generations ( $N_{gen}$ ), number of parents ( $N_{par}$ ), elitism count ( $N_{elite}$ ), and mutation rate ( $f_{mut}$ ) were scaled with  $d$ , to maintain adequate search coverage and genetic diversity. Convergence was monitored using the stopping criterion,  $\mathcal{T}_{stop}$ , which terminated the optimisation once the fitness improvement plateaued. Detailed heuristic ranges for these parameters are provided in Appendix A.1.

### 2.2.2. Bayesian Optimisation

An alternative global optimisation strategy, Bayesian optimisation (BO), is used to efficiently search the design space by using results from COMSOL simulations to

train a Gaussian Process (GP) surrogate model of  $F(\mathbf{x})$  across the design space. This approach reduces the number of required simulations by guiding the search toward promising regions of the parameter space.

The GP uses a Matérn covariance kernel with smoothness parameter  $\nu = 2.5$ , implemented via the `GaussianProcessRegressor` in `scikit-learn` [53], with automatic optimisation of the kernel hyperparameters (signal variance and length scale). The Matérn kernel defines how the correlation between two design points decays with distance in parameter space and determines the smoothness of the surrogate function. Automatic hyperparameter optimisation ensures that the kernel parameters adapt to the scale and variability of the underlying COMSOL data at each iteration.

An initial set of  $N_{init} = 3000$  points is sampled uniformly within the normalised design space ( $\mathbf{x}$ ) and evaluated in COMSOL to form a training dataset  $\{\mathbf{x}_i, F(\mathbf{x}_i)\}$ . The GP is then trained to predict both the mean and uncertainty of  $F(\mathbf{x})$  at untested geometries. New candidates are selected by maximising the Expected Improvement (EI) acquisition function, which balances exploration of uncertain regions and exploitation of high-performing areas. EI maximisation is performed using the L-BFGS-B algorithm with multiple random restarts,  $N_{restart} = 10$ , within the same bounds.

At each iteration, one new geometry is selected, evaluated using COMSOL, and added to the dataset. The GP is retrained with the updated data, and the process repeats until the maximum number of iterations ( $N_{BO} = 200$ ) is reached. The best-performing BO design corresponds to the highest  $F(\mathbf{x})$  observed over all evaluations. The GP predictive standard deviation,  $\sigma_{pred}$ , is analysed over  $N_{test} = 2000$  random samples in  $\mathbf{x}$  to quantify model confidence and coverage of the explored design space.

While both GA and BO optimise over the same geometric parameter set and use the same  $F(\mathbf{x})$ , they differ fundamentally in their search strategies: GA explores the space through stochastic sampling and evolutionary pressure, whereas BO constructs a statistical model of the fitness landscape to efficiently target regions of high performance.

### 2.3. Mesh Convergence

To verify that the value of  $|\mathcal{H}_m|$  for each optimised cavity reflects genuine geometric effects rather than artefacts of mesh discretisation, mesh-convergence testing was performed for the optimised cavity in each cavity family. Mesh convergence was assessed via a parametric sweep of the maximum mesh element size, confirming that the FoM stabilised under successive refinement. Convergence was quantified by evaluating the relative change in  $F(\mathbf{x})$  between consecutive meshes and verifying that it fell below a 0.001% threshold. This ensures that the reported FoM values are insensitive to mesh size.

### 2.4. Optimised Cavity Performance Metrics

The performance of the optimised cavity from each cavity family is characterised using a set of key metrics, including the resonant frequency  $f_i$ ,  $|\mathcal{H}_i|$ , surface-loss, and robustness to perturbations. To enable fair comparison between distinct cavity families, all models are uniformly scaled to maintain a constant surface-to-volume ratio prior to eigenmode analysis.

Surface-loss performance is quantified by the geometric factor,  $G$ , which characterises the sensitivity of a resonant mode to dissipation at the conducting walls and is defined for a given mode  $i$  as [54]:

$$G_i = 2\pi f_i \frac{\iiint_V \mu_0 |\vec{\mathbf{H}}_i|^2 dv}{\iint_S |\vec{\mathbf{H}}_i^\tau|^2 ds}, \quad (4)$$

where  $\mu_0$  is the vacuum permeability. The volume integral is taken over the cavity volume  $V$ , while the surface integral evaluates the tangential magnetic field  $\vec{\mathbf{H}}_i^\tau$  over the conducting walls. Physically, a larger  $G$  indicates reduced sensitivity to surface losses, as the mode stores a greater fraction of its electromagnetic energy away from the cavity walls, thereby suppressing surface-induced dissipation.  $G$  is related to the intrinsic quality factor,  $Q_0$ , through [50]:

$$Q_0 = \frac{G}{R_S}, \quad (5)$$

where  $R_S$  denotes the surface resistance. To enable comparison between cavity families, for which the most helical mode occurs at different resonant frequencies, we define the frequency-normalised geometric factor

$$\tilde{G}_i = \frac{G_i}{2\pi f_i \mu_0}, \quad (6)$$

which isolates the purely geometric contribution to surface-loss performance.

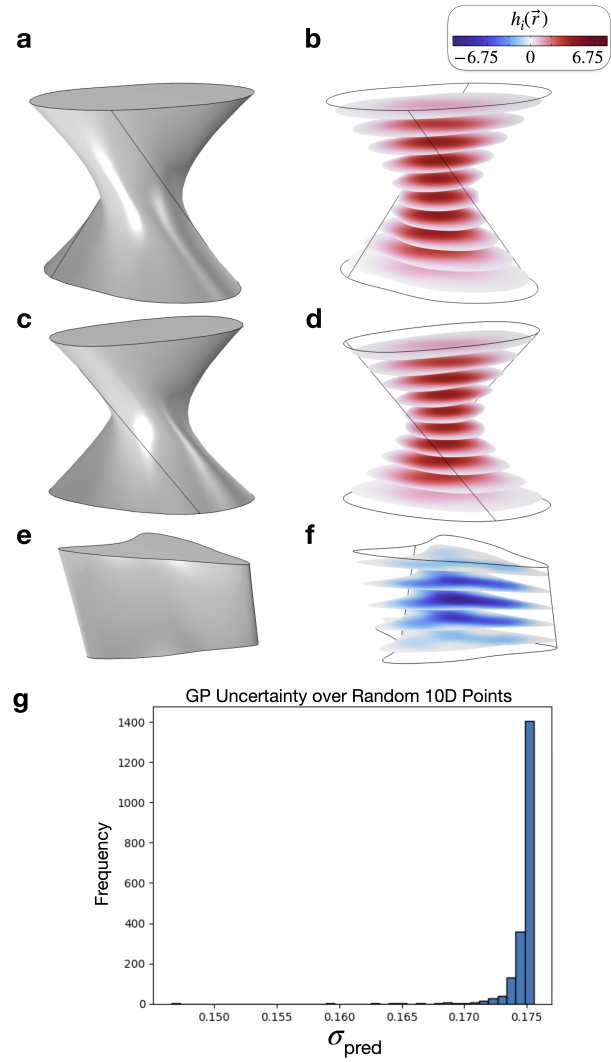


FIG. 2. (A) GA-optimised EF twisted linear cavity geometry and (B) its corresponding  $h_i(\vec{r})$  field distribution. (C) BO-optimised cavity and (D) its corresponding  $h_i(\vec{r})$  field distribution. (E) GA-optimised expanded-radius variant and (F) its corresponding  $h_i(\vec{r})$  field distribution. (G) Histogram of  $\sigma_{\text{pred}}$  across 2,000 random points in the 10D input space.

To evaluate how small perturbations in the high-dimensional parameter set defining the optimised cavity geometry affect  $F(\mathbf{x})$ , each parameter of the optimised geometry  $\mu_j$  is treated as subject to independent Gaussian uncertainty with a prescribed standard deviation  $\sigma_j$ , representing a perturbation on the order of 1% in the normalised design space. In practice, these uncertainties represent the fabrication tolerances inherent to AM parts and electropolishing, as discussed in the introduction. They also capture geometric errors that may arise from post-fabrication assembly effects, such as misalignment, assembly-induced strain or deformation, and probe-induced perturbations.

Direct random sampling of these uncertainties would

TABLE 2. Parameters for the optimised cavities in the EF twisted family.

Geometry	Optimisation	$H$ (mm)	$\theta$ (rad)	$\{r_i\}$ (mm)
EF twisted linear (baseline) [Sec. 3.1]	GA	48.6	1.94	{22.9, 17.9, 22.7, 31.6, 25.1, 19.2, 24.7, 30.9}
	BO	44.5	1.96	{25.9, 29.0, 19.7, 18.6, 25.4, 28.3, 19.6, 19.6}
EF twisted linear (expanded $r_i$ )	GA	35.2	0.716	{21.0, 40.5, 23.1, 20.4, 38.1, 19.9, 23.1, 39.8}
EF twisted ring [Sec. 3.2]	GA	995	$10\pi$	{30.8, 17.4, 25.9, 19.5, 15.6, 29.0, 17.4, 16.5}

TABLE 3. Statistical robustness metrics for the GA-optimised cavities under Gaussian perturbations.

Geometry	$\bar{F}$	$\sigma_F$	$F_{0.05}$	$F_{\min}$	$\mathcal{R}$
EF twisted linear (baseline) [Sec. 3.1]	1.02	0.0024	1.02	1.01	1.02
EF twisted linear (expanded $r_i$ )	0.931	0.148	0.708	0.685	0.635
EF twisted ring [Sec. 3.2]	1.44	0.0767	1.33	0.978	1.29
Orthogonal prism-intersection [Sec. 3.3]	0.859	0.0620	0.691	0.621	0.735
Sphere-subtracted cylindrical [Sec. 3.4]	0.867	0.0800	0.699	0.598	0.707
Parametrised surface [Sec. 3.5]	0.495	0.191	0.283	0.279	0.113

leave large gaps in the multidimensional tolerance space when only  $N \approx 10^2$  model evaluations are feasible, so Latin Hypercube Sampling (LHS) was used to ensure even sampling across the uncertainty range of each nominal parameter  $\mu_j$ . Each uniform draw  $u_{sj} \in (0, 1)$  is mapped through the inverse normal cumulative distribution,  $\Phi^{-1}(u_{sj})$ , to generate perturbed parameter vectors  $x_{sj} = \mu_j + \sigma_j \Phi^{-1}(u_{sj})$ , producing an ensemble  $\{\mathbf{x}_s\}_{s=1}^N$  drawn from  $\mathcal{N}(\boldsymbol{\mu}, \text{diag } \boldsymbol{\sigma}^2)$  while sampling the design space efficiently. A fixed random seed (`seed=42`) was used to initialise the pseudorandom number generator that controls the LHS, allowing the same ensemble of perturbed geometries to be regenerated for reproducibility.

The FoM was evaluated for each perturbed geometry  $\mathbf{x}_s$  in COMSOL, yielding a distribution of values  $\{F(\mathbf{x}_s)\}$  that quantifies how machining tolerances influence performance. The mean  $\bar{F}$  and standard deviation  $\sigma_F$  describe the central tendency and variability, while the 5th percentile  $F_{0.05}$  and the minimum value  $F_{\min}$  indicate the near- and worst-case outcomes. A robustness index,  $\mathcal{R} = \bar{F} - 2\sigma_F$ , combines average performance and variability, penalising designs whose  $F(\mathbf{x})$  fluctuates strongly under perturbation and providing a single measure of geometric tolerance. This framework enables direct comparison between competing geometries and a clear assessment of their resilience to fabrication imperfections.

### 3. GEOMETRIES

#### 3.1. Edge-Free Twisted Linear Cavity

The previously investigated twisted prism resonators [14–17], which employ cross-sections with  $D_n$  symmetry as discussed in the Introduction, were fabricated via additive manufacturing of twisted prism waveguides and subsequently terminated with separately manufactured electrically conducting endcaps to form cavities. However, the polygonal cross-sections of these designs introduce sharp edges and internal corners, and therefore inherit the surface-treatment limitations discussed in the Introduction.

To overcome these limitations, the present approach employs smoothly varying, closed 2D interpolation curves in lieu of polygonal profiles for the additively manufactured waveguide. Each curve is defined by  $n = 8$  control points whose Cartesian coordinates are  $(r_i \cos \varphi_i, r_i \sin \varphi_i)$ , with fixed angular positions  $\varphi_i = 2\pi i/n$  and radial distances  $r_i$  treated as optimisation variables. The resulting planar shape is then lofted into three dimensions by extrusion over a height  $H$ , with a uniformly distributed total twist angle  $\theta$  applied along the height. The free parameters defining the design space, along with their respective ranges, are therefore  $\theta \in [0, 2\pi]$ ,  $H \in [26, 156]$  mm, and  $r_i \in [15, 33]$  mm.

The tetrahedral mesh used for this configuration employed a maximum element size of 2.53 mm and a minimum element size of 0.108 mm. A maximum element growth rate of 1.35 was used, together with a curvature factor of 0.3. The narrow-region resolution was set to 0.85.

The optimisation was performed using both the GA and BO frameworks. For each candidate geometry, an eigenvalue analysis was carried out to compute 44 eigenfrequencies in the vicinity of 10 GHz, from which the values of  $|\mathcal{H}_i|$  for the supported modes were evaluated.

The parameters of the optimised geometries are listed in Table 2. The GA-optimised geometry and the corresponding  $h_i(\vec{r})$  field distribution of its resonant mode are shown in Fig. 2(a) and (b), respectively, yielding  $\tilde{G}_i =$

5.26 mm and  $\mathcal{H}_i = 1.03$ . The BO-optimised counterpart, shown in Fig. 2(c) and (d), achieves  $\tilde{G}_i = 4.57$  mm and  $\mathcal{H}_i = 1.02$ . Both optimisation frameworks yield cavities that converge to similarly high  $|\mathcal{H}_i|$  values, approaching the upper bound attainable within this design space.

Expanding the admissible range of the control-point radii to  $r_i \in [5, 59]$  mm yields a second GA-optimised F twisted linear cavity that achieves  $\mathcal{H}_i = 1.100$  and  $\tilde{G}_i = 6.32$  mm (see Table 2 for the optimised cavity parameters). The optimised geometry and its corresponding  $h_i(\vec{r})$  distribution are shown in Fig. 2(e) and (f), respectively.

The statistical robustness metrics for the GA-optimised EF twisted linear cavity, optimised over the baseline and expanded- $r_i$  design spaces, are summarised in the first two rows of Table 3. The baseline geometry exhibits a very low  $\sigma_F$  and a near-unity  $\mathcal{R}$ , demonstrating excellent stability of  $|\mathcal{H}_i|$  under parametric perturbations. By contrast, the expanded-radius geometry attains higher  $|\mathcal{H}_i|$  and  $\tilde{G}_i$  at the expense of a substantially broader fitness distribution and reduced  $\mathcal{R}$ , reflecting increased sensitivity to geometric perturbations arising from large radial excursions and revealing a clear trade-off between maximising the degree of  $|\mathcal{H}_i|$  supported and maintaining robustness to fabrication or alignment variations.

For the BO-optimised surrogate model, predictive uncertainty was evaluated using the trained GP. The histogram in Fig. 2(g) shows the distribution of  $\sigma_{\text{pred}}$ , across 2,000 random points in the 10D design space, which is sharply peaked around 0.175. This indicates that the GP is confident and well-calibrated throughout the explored region, reinforcing the reliability of the BO-generated solution.

Both the GA and BO approaches converge to near-identical  $|\mathcal{H}_i|$  values. However, the GA achieves a marginally higher result, with a 0.589% increase in  $|\mathcal{H}_i|$ . This difference arises from the broader sampling of the parameter space inherent to the GA approach.

### 3.2. Edge-Free Twisted Ring Cavity

The EF twisted linear cavity described previously was further examined in a ring configuration, created by bending the underlying waveguide into a continuous closed loop. The total twist angle was constrained to discrete values of  $\theta = 2\pi m$ ,  $m \in \{0, 1, \dots, 8\}$ , ensuring that the waveguide's end faces joined seamlessly.

For this geometry, the tetrahedral mesh parameters were set to a maximum element size of 4.89 mm and a minimum element size of 0.209 mm. A maximum element growth rate of 1.35 was used, together with a curvature factor of 0.3. The narrow-region resolution was set to 0.85.

The optimisation was performed using the GA framework. For each candidate geometry, an eigenvalue analy-

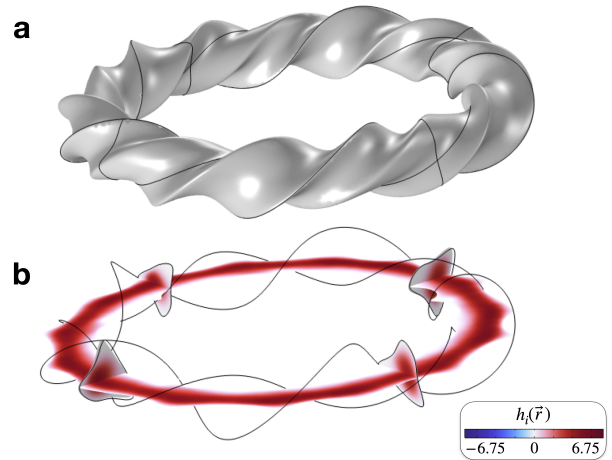


FIG. 3. (A) The optimised EF twisted ring cavity and (B) its  $h_i(\vec{r})$  field distribution.

sis was carried out to compute 35 eigenfrequencies in the vicinity of 10 GHz in order to optimise for the largest possible  $|\mathcal{H}_i|$ .

The optimisation identified the configuration in Fig. 3(a) as the highest-performing design, with the corresponding  $h_i(\vec{r})$  field depicted in Fig. 3(b). The geometric parameters associated with this optimised cavity are shown in Table 2. The cavity achieves a very high  $|\mathcal{H}_i|$  of 1.47 and  $\tilde{G}_i$  of 14.2 mm.

The statistical robustness metrics for the GA-optimised EF twisted ring cavity under Gaussian geometric perturbations are summarised in Table 3. The very high  $\bar{F}$  and  $\mathcal{R}$  values indicate that the EF twisted ring cavity maintains large  $|\mathcal{H}_i|$  even under geometric perturbations.

### 3.3. Orthogonal Prism-intersection Cavity

The orthogonal prism-intersection cavity geometry is generated by taking the volumetric intersection of two effectively infinite, untwisted waveguides whose cross-sectional boundaries are defined by closed  $n$ -point interpolation curves ( $n = 8$ ). Each curve lies in a transverse plane and is parameterised by radial distances  $r_i$  (for the first prism) or  $v_i$  (for the second) at fixed azimuthal angles  $\varphi_i = 2\pi i/n$ , consistent with the definition used in the previous section. Both prisms are assigned a length ( $H = 100$  mm) much greater than their transverse dimensions so that end-cap effects become negligible. The cavity is then defined by the resulting intersection volume, which is fully determined by the two sets of radii  $\{r_i\}$  and  $\{v_i\}$ . The free parameters defining the design space explored by the GA are the individual radii comprising these sets, each subject to the bounds  $r_i \in [13, 33]$  mm and  $v_i \in [13, 33]$  mm.

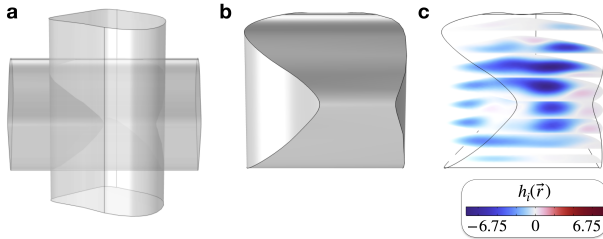


FIG. 4. (A) Two infinitely long, untwisted waveguides whose cross-sectional boundaries define (B) the optimised orthogonal prism-intersection cavity. (C) The corresponding  $h_i(\vec{r})$  field distribution.

For this geometry, the tetrahedral mesh parameters were set to a maximum element size of 1.82 mm and a minimum element size of 0.132 mm. A maximum element growth rate of 1.4 was used, together with a curvature factor of 0.4. The narrow-region resolution was set to 0.7.

The optimisation was performed using the GA framework. For each candidate geometry, 44 eigenfrequencies near 10 GHz were computed to evaluate the  $|\mathcal{H}_i|$  of the supported eigenmodes.

The construction process and resulting geometry of the optimised orthogonal prism-intersection cavity are illustrated in Fig. 4(a) and (b), with the  $h_i(\vec{r})$  distribution of the resonant mode shown in Fig. 4(c). The corresponding optimised cavity parameters are  $\{r_i\} = \{19.6, 15.9, 28.9, 18.3, 21.8, 21.9, 31.1, 32.5\}$  mm and  $\{v_i\} = \{33.0, 19.2, 19.0, 13.5, 20.8, 31.5, 30.7, 22.2\}$  mm. This design achieved a  $\mathcal{H}_i = -0.9$  and a  $\tilde{G}_i = 8.27$  mm.

The statistical robustness metrics for the GA-optimised orthogonal prism-intersection resonator under Gaussian geometric perturbations are summarised in Table 3. On average, the cavity maintained a high  $|\mathcal{H}_i|$ , though it exhibits only moderate robustness to geometric perturbations. This sensitivity arises because even small changes to the underlying cylindrical shapes significantly alter the intersection boundary that defines the cavity, which in turn strongly affects the helical field pattern.

### 3.4. Sphere-Subtracted Cylindrical Cavity

A baseline cylindrical resonator of height  $H$  and radius  $R$  is first defined, with both treated as optimisation variables. Around the cylinder's top and bottom rims, a set of  $n$ -spherical voids is introduced ( $n = 8$ ), each described by its radius,  $r_i$ , radial offset from the central axis,  $dr_i$ , and azimuthal angle,  $\phi_i$ . The centres of spheres  $i = 1-4$  are positioned a distance  $H_1 = 10$  mm above the top rim, while those of spheres  $i = 5-8$  are placed a distance  $H_1$  below the bottom rim. The cavity geometry is then obtained by subtracting the union of these spheres from the solid cylinder. The design space for this cavity family is

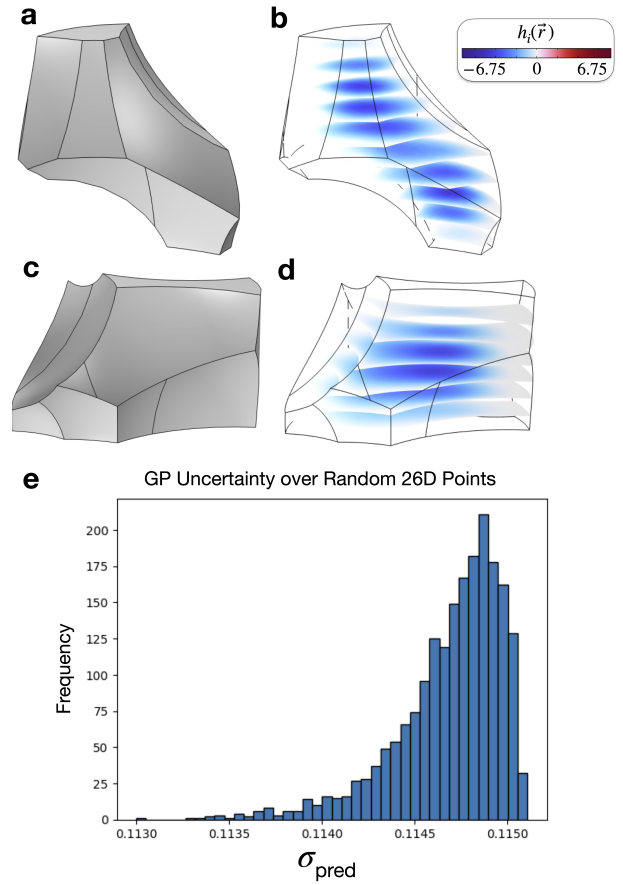


FIG. 5. (A) GA-optimised cavity based on sphere-subtracted sculpted cylinders and (B) its corresponding  $h_i(\vec{r})$  field distribution. (C) BO-optimised cavity and (D) its corresponding  $h_i(\vec{r})$  field distribution. (E) Histogram of  $\sigma_{\text{pred}}$  across 2,000 random points in the 26D input space.

therefore defined by the free parameters, along with their respective ranges,  $H \in [40, 70]$  mm,  $R \in [20, 40]$  mm,  $\phi_i \in [0, 2\pi]$ ,  $r_i \in [20, 55]$  mm, and  $dr_i \in [5, 30]$  mm.

The tetrahedral mesh used for this geometry employed a maximum element size of 3 mm and a minimum element size of 0.2 mm. A maximum element growth rate of 1.4 was used, together with a curvature factor of 0.4. The narrow-region resolution was set to 0.7.

The optimisation was performed using both the GA and BO framework. For each candidate geometry, 41 eigenfrequencies near 5 GHz were computed to evaluate the corresponding  $|\mathcal{H}_i|$  values.

The GA-optimised configuration is shown in Fig. 5(a), with the corresponding  $h_i(\vec{r})$  field distribution depicted in Fig. 5(b). This design achieved a  $\mathcal{H}_i$  of  $-0.958$  and a  $\tilde{G}_i$  of  $3.83$  mm. In comparison, BO applied to the same parameter space yielded an optimised resonator with  $\mathcal{H}_i = -0.750$  and  $\tilde{G}_i = 7.38$  mm. The geometry of this resonator is shown in Fig. 5(c), and the corresponding  $h_i(\vec{r})$  field is shown in Fig. 5(d). The parameters of

TABLE 4. Optimised parameters for the sphere-subtracted cylindrical resonator obtained using GA and BO.

Optimisation	$H$	$R$	$\{\phi_i\}$	$\{r_i\}$ (mm)	$\{dr_i\}$ (mm)
GA	41.0	20.7	{1.08, 1.80, 3.21, 4.74, 2.66, 5.28, 4.16, 3.22}	{29.9, 36.1, 49.9, 30.5, 47.1, 34.0, 49.1, 53.6}	{5.42, 20.1, 19.2, 23.3, 23.3, 11.9, 18.3, 24.3}
BO	39.2	47.0	{4.76, 3.22, 0.609, 3.77, 0.756, 4.32, 2.65, 3.89}	{54.7, 31.0, 45.6, 41.6, 50.0, 54.7, 51.6, 23.0}	{20.2, 12.7, 28.4, 14.2, 22.3, 12.5, 17.3, 23.3}

these optimised geometries are summarised in Table 4.

While both optimisation methods produce large  $|\mathcal{H}_i|$ , the GA-optimised geometry achieves a 27.7% higher value, whereas its  $\tilde{G}_i$  is only half that of the BO-optimised design. This difference in  $|\mathcal{H}_i|$  and  $\tilde{G}_i$  arises from their differing search strategies: GA samples the true, potentially rugged fitness landscape and can access narrow, high-variance regions where strong field hybridisation and sharper curvature enhance  $|\mathcal{H}_i|$  but also increase surface area, concentrating magnetic-field intensity near the conducting walls and lowering  $\tilde{G}_i$ . In contrast, BO relies on a smooth Gaussian-process surrogate that favours broad, slowly varying regions of parameter space, yielding geometries with gentler curvature.

The statistical robustness metrics for the GA-optimised sphere-subtracted cylindrical resonator under Gaussian geometric perturbations are summarised in Table 3. The  $\bar{F}$  and  $\mathcal{R}$  values indicate that the sphere-subtracted cylindrical resonator maintains high  $|\mathcal{H}_i|$  on average but exhibits moderate sensitivity to geometric perturbations. This sensitivity to geometric perturbations likely arises from sharper geometric transitions inherent to the sphere-subtracted cylindrical design, which amplify local field variations under perturbation.

For the BO-optimised surrogate, predictive uncertainty was evaluated over 2,000 random samples in the 26D design space. As shown in Fig. 5(e), the predicted standard deviations are tightly clustered between 0.114 and 0.115, with most values near the upper end of this narrow range. This near-uniformity confirms that the GP model is well-calibrated and confident across the explored region.

### 3.5. Parameterised Surface Cavity

Two parametric surfaces, separated by  $z_1 = 0.5$  mm, are defined by a dimensionless parameter domain  $s_1, s_2 \in [-1, 1]$ . The surfaces are described by

$$\vec{r}_1(s_1, s_2) = \left( s_1, s_2, p_1 \cos(\pi s_1) \sin(\pi s_2) + p_2 s_1 s_2 e^{-s_1^2 - s_2^2} + p_3 \cos(\pi s_1 s_2) \right) \text{ mm}, \quad (7)$$

$$\vec{r}_2(s_1, s_2) = \left( s_1, s_2, p_4 \cos(\pi s_1) \sin(\pi s_2) + p_5 s_1 s_2 e^{-s_1^2 - s_2^2} + p_6 \cos(\pi s_1 s_2) \right) \text{ mm}, \quad (8)$$

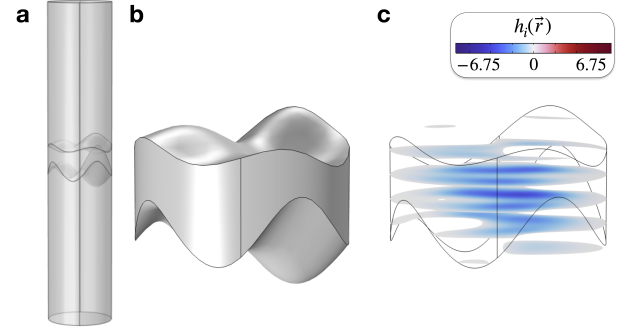


FIG. 6. (A) The original unmodified parameterised surfaces and cylinder, alongside (B) the optimised cavity formed from parameterised surfaces, and (C) the corresponding  $h_i(\vec{r})$  field distribution.

where each  $p_i \in [-1, 1]$  mm controls the out-of-plane deformation of the surface. The cavity geometry is defined as the solid volume of a cylinder of radius 1 mm whose upper and lower faces are replaced by the two parametric surfaces  $\vec{r}_1$  and  $\vec{r}_2$  over the domain  $s_1, s_2 \in [-1, 1]$ . This volume is then uniformly scaled by a factor of 13 in all spatial dimensions.

The tetrahedral mesh used for this configuration employed a maximum element size of 0.91 mm and a minimum element size of 0.039 mm. A maximum element growth rate of 1.35 was used, together with a curvature factor of 0.3. The narrow-region resolution was set to 0.85.

The optimisation was performed using the GA framework. For each candidate geometry, 44 eigenfrequencies in the vicinity of 10 GHz were computed to evaluate  $|\mathcal{H}_i|$ .

The surface-based construction method used to generate this optimised geometry is illustrated in Fig. 6(a), the resulting structure is shown in Fig. 6(b) and the corresponding  $h_i(\vec{r})$  distribution is shown in Fig. 6(c). The optimised geometry corresponds to the parameter set  $\{p_i\} = \{-0.384, -0.864, -0.381, -0.192, -0.808, 0\}$  mm. This cavity achieves  $\mathcal{H}_i = -0.673$  and  $\tilde{G}_i = 2.90$  mm, indicating that this cavity family exhibits intrinsically low  $|\mathcal{H}_i|$  and cannot be optimised toward the upper bound of  $|\mathcal{H}_i|$ .

The statistical robustness metrics for the GA-optimised parameterised surface under Gaussian geometric perturbations are summarised in Table 3. The low  $\mathcal{R}$  value indicates that the performance of the parameterised

TABLE 5. Summary of the performance metrics of the optimised cavity geometries, showing the mode frequency  $f_i$ , electromagnetic helicity  $\mathcal{H}_i$ , frequency-normalised geometric factor  $\tilde{G}_i$ , and robustness index  $\mathcal{R}$ . The cylindrical cavity resonators use the same geometric dimensions as those reported in Ref. [50], with  $f_i$  and  $G_i$  computed independently and in agreement with the published values within numerical tolerance. The linear twisted  $D_3$  resonators correspond to the geometry studied in Refs. [14, 15], evaluated here at a twist angle of  $\theta = 10\pi/9$ .

Cavity	Optimisation	$f_i$ (GHz)	$\mathcal{H}_i$	$\tilde{G}_i$ (mm)	$\mathcal{R}$
EF twisted linear (baseline) [Sec. 3.1]	GA	8.57	1.03	5.26	1.02
	BO	9.15	1.02	4.57	—
EF twisted linear (expanded $r_i$ )	GA	9.42	1.10	6.32	0.635
EF twisted ring [Sec. 3.2]	GA	9.99	1.47	14.2	1.29
Orthogonal prism-intersection [Sec. 3.3]	GA	12.0	-0.900	8.27	0.735
Sphere-subtracted cylindrical [Sec. 3.4]	GA	17.1	-0.958	3.83	0.707
	BO	6.23	-0.750	7.38	—
Parametrised surface [Sec. 3.5]	GA	20.0	-0.673	2.90	0.113
Cylinder (TM <sub>0,1,0</sub> )	—	11.2	0	3.78	—
Cylinder (TE <sub>0,1,1</sub> )	—	18.6	0	5.15	—
Linear twisted $D_3$	—	16.9	0.925	2.16	—

surface deteriorates substantially under small geometric deviations. This sensitivity to small geometric deviations arises from its highly variable surface topology, where even minor parameter shifts induce significant field distortions and reduce the stability of the chiral response.

#### 4. DISCUSSION

Inverse design enabled the discovery of fully 3D microwave cavities that support highly chiral eigenmodes, achieved by directly optimising cavity boundaries to maximise  $|\mathcal{H}_i|$ . This approach uncovers resonator geometries that would be difficult to anticipate through conventional, intuition-driven design methods and, in several cases, achieves surface-loss performance comparable to or exceeding that of standard cavity designs. All optimised cavity geometries are summarised in Table 5, which also includes benchmark cylindrical cavity modes, TM<sub>0,1,0</sub> and TE<sub>0,1,1</sub>, corresponding to the TM and TE modes of a cavity with an equal surface-to-volume ratio, as well as the fundamental helical mode of the twisted linear  $D_3$  resonator with a twist angle of  $\theta = 10\pi/9$  [14, 15].

Among all designs, the EF twisted resonator family consistently delivers the highest  $|\mathcal{H}_i|$ , owing to their global, continuous twist, which maintains a uniform spatial overlap of parallel components of  $\vec{E}$  and  $\vec{H}$  throughout the volume. As a result,  $h_i$  integrates constructively over the entire cavity. The ring configuration of this resonator family emerges as the top performer across all metrics. Bending the linear geometry into a closed loop eliminates the metallic endcaps which would otherwise disrupt the uniform spatial overlap of  $\vec{E}$  and  $\vec{H}$ , producing a larger  $|\mathcal{H}_i|$ . Their removal also eliminates sharp reflection planes, enforcing continuous boundaries around the cavity. Perturbations therefore act globally rather than being concentrated at end surfaces, enhancing  $\mathcal{R}$ .

The EF twisted linear resonator with modest bounds on the admissible range of control-point radii  $r_i$ , how-

ever, remains a strong performer and is easier to fabricate, as it avoids the need for seamless joining. While its  $\tilde{G}_i$  is only 1.39 times that of the TM<sub>0,1,0</sub> mode in a cylindrical cavity, the ring resonator achieves a substantially higher  $\tilde{G}_i$  of 3.76 times that of the TM<sub>0,1,0</sub> mode. This increase also arises from the elimination of the metallic endcaps, which reduces magnetic field confinement near the conducting walls and therefore lowers surface loss. Expanding the allowable range of control-point radii can further increase  $|\mathcal{H}_i|$ , but this enhancement arises from large radial excursions rather than global twist, making such helical modes more sensitive to dimensional variation.

The orthogonal prism-intersection resonator is another high-performing design, exhibiting a  $\tilde{G}_i$  higher than that of the EF twisted linear resonator and approximately 2.19 times that of the TM<sub>0,1,0</sub> mode. Its favourable  $\tilde{G}_i$  arises from the absence of deep recesses or sharply varying curvature that could pull the magnetic field towards the conducting walls, allowing for less surface-loss. This resonator also supports a strong  $|\mathcal{H}_i|$  and moderate  $\mathcal{R}$ . The moderate sensitivity to geometric variations likely stems from the fact that the  $|\mathcal{H}_i|$  is generated by local curvature variations rather than a global twist; such locally induced features are more susceptible to perturbations.

By contrast, the parameterised-surface resonator performs the worst across all metrics. Its deep, irregular curvature disrupts constructive integration of  $h_i$  throughout the volume, suppressing  $|\mathcal{H}_i|$ , and draws the magnetic field toward the conducting boundaries, reducing  $\tilde{G}_i$ .

The sphere-subtracted cylindrical resonator exhibits moderately high  $|\mathcal{H}_i|$ , but a low  $G_i$  and only moderate  $\mathcal{R}$ . In this case, the  $|\mathcal{H}_i|$  arises from sharp, highly varying complex features and recesses that concentrate the magnetic field near the conducting walls, lowering  $G_i$ . Because the mode is supported by these intricate local features, it is also more susceptible to small geometric deviations, which reduce  $\mathcal{R}$ .

The machine learning optimisation identified highly helical modes in most cavity families, generated through two distinct mechanisms. The first mechanism arises in complex geometries containing sharp and/or rapidly varying curvature. In these designs, strong  $|\mathcal{H}_i|$  is produced through the local curvature of these features. However, such  $|\mathcal{H}_i|$  is inherently fragile: even small geometric deviations disrupt the localised spatial overlap of  $\vec{E}$  and  $\vec{H}$ , leading to a reduced  $\mathcal{R}$ . As a result, although these geometries can exhibit high  $|\mathcal{H}_i|$ , they do so at the expense of  $\mathcal{R}$ . Their  $\tilde{G}_i$  is sensitive to the depth of these features. Deep recesses pull a larger fraction of the magnetic field toward the conducting walls, increasing surface losses that lower  $\tilde{G}_i$  as well as amplifying sensitivity to geometric perturbations.

The second mechanism occurs in geometries with a global, continuous twist. Here, the  $|\mathcal{H}_i|$  arises from a smooth global curvature that maintains a consistent spatial overlap of  $\vec{E}$  and  $\vec{H}$  along the entire structure. Therefore,  $h_i$  integrates constructively throughout the full cavity volume, producing high  $|\mathcal{H}_i|$  without relying on delicate local features. Because the  $|\mathcal{H}_i|$  is reinforced globally rather than locally, these designs are far less sensitive to dimensional variations and therefore exhibit a superior  $\mathcal{R}$ . The strongest performers across all metrics are those with continuous boundaries and no sharp reflection planes or discontinuities. These results highlight the advantage of global twist over highly complex geometries when  $\mathcal{R}$  is a key design requirement.

Comparing the performance of the GA- and BO-optimised cavities in Table 5, it is evident that the GA identified solutions with higher  $|\mathcal{H}_i|$  than BO, as also noted in Sec. 3.4. This demonstrates the benefit of broad, stochastic search strategies when navigating complex 3D parameter spaces.

## CONCLUSION

In this work, we demonstrated that a machine-learning-driven inverse design framework provides a systematic route to engineering microwave cavity resonators with large electromagnetic helicity,  $|\mathcal{H}_i|$ , surpassing the performance of previously studied heuristically designed twisted cavities with  $D_3$  symmetry [14–17]. By formulating  $|\mathcal{H}_i|$  maximisation as a boundary-shape optimisation problem and exploring the resulting design space using gradient-free optimisation strategies, the framework enables efficient exploration of complex, high-dimensional boundary parameter spaces. Unlike conventional heuristic design approaches, which rely on physical intuition and incremental geometric modification, this approach systematically uncovers resonator geometries composed of smooth, edge-free components that support strongly helical modes.

The 3D microwave resonators obtained via inverse design not only achieve higher  $|\mathcal{H}_i|$  than hand-crafted resonators, but also exhibit improved surface-loss perfor-

mance and strong robustness to realistic geometric perturbations, maintaining resilience to fabrication-induced imperfections such as those introduced by additive manufacturing. In contrast to most inverse design efforts in photonics that focus on quasi-2D structures, our framework operates on fully 3D metallic microwave cavities that are compatible with additive fabrication techniques.

This same framework can be adapted to alternative or composite figures of merit, such as gradients of fields or joint optimisation of  $|\mathcal{H}_i|$  and  $\tilde{G}_i$ , providing a flexible path toward tailored chiral-field engineering. Machine learning therefore provides a general and scalable pathway for the systematic design of highly chiral, low-loss microwave resonators with complex 3D metallic boundaries that are manufacturable and can be tailored to applications in enantioselective spectroscopy, parity-violation experiments, axion haloscopes, and beyond.

## ACKNOWLEDGEMENTS

This work was funded by the Australian Research Council Centre of Excellence for Engineered Quantum Systems (CE170100009) and the Centre of Excellence for Dark Matter Particle Physics (CE200100008).

## APPENDICES

### A.1. Heuristic Scaling of Genetic Algorithm Parameters

The genetic algorithm (GA) parameters used in this study were empirically tuned to ensure robust convergence across optimisation spaces of varying dimensionality  $d$ , implemented using the PyGAD Python Genetic Algorithm framework. The population size,  $N_{\text{pop}}$ , was typically set between  $(5 \dots 10) \times d$  to maintain genetic diversity, while practical values ranged from  $(2 \dots 14) \times d$  depending on computational limits. The number of generations,  $N_{\text{gen}}$ , was increased with  $d$  to ensure convergence in higher-dimensional design spaces, generally spanning 50 to 200 generations. The number of parents,  $N_{\text{par}}$ , determined how many of the top-performing individuals contributed to the next generation and was scaled with the population size to preserve crossover diversity. Elitism,  $N_{\text{elite}}$ , specified the number of top individuals preserved unchanged between generations and was kept approximately constant as a fraction of the total population (typically 20–25%), except where reduced to manage computational load. A summary of how these variables correspond to the underlying PyGAD parameter names is given in Table A1.

The mutation strength,  $\sigma_{\text{mut}}$ , as defined in the main text (see Sec. 2), typically ranged between 0.08–0.18

across cavity families to balance exploration and stability. The mutation rate,  $f_{\text{mut}}$ , controlled the fraction of genes modified per generation and was set between 10–35%, with higher values applied to geometries requiring broader exploration or exhibiting more complex optimisation landscapes.

A "single-point" crossover and "tournament" parent selection (size 3) were employed consistently across all optimisations, as these parameters primarily affect selection pressure rather than dimensionality. Convergence was monitored using a stopping criterion,  $T_{\text{stop}}$ , based on either fitness thresholds or saturation conditions (e.g., "reach\_98" or "saturate\_7-40"), ensuring termination once optimisation progress plateaued.

TABLE A1. Mapping between the notation used in this work and the corresponding PyGAD parameters.

Manuscript Notation	PyGAD Parameter
Design dimensionality $d$	<code>num_genes</code>
Population size $N_{\text{pop}}$	<code>sol_per_pop</code>
Number of generations $N_{\text{gen}}$	<code>num_generations</code>
Number of parents $N_{\text{par}}$	<code>num_parents_mating</code>
Elitism count $N_{\text{elite}}$	<code>keep_elitism</code>
Mutation rate $f_{\text{mut}}$	<code>mutation_percent_genes/100</code>
Stopping criterion $T_{\text{stop}}$	<code>stop_criteria</code>

---

[1] L. Su, D. Vercruyse, J. Skarda, N. V. Sapra, J. A. Petykiewicz, and J. Vučković, *Applied Physics Reviews* **7**, 011407 (2020).

[2] A. Y. Piggott, J. Petykiewicz, L. Su, and J. Vučković, *Scientific Reports* **7**, 1786 (2017), arXiv:1612.03222 [physics.optics].

[3] M. F. Schubert, A. K. C. Cheung, I. A. D. Williamson, A. Spyra, and D. H. Alexander, *ACS Photonics* **9**, 2327 (2022), <https://doi.org/10.1021/acsphotonics.2c00313>.

[4] L. Su, A. Y. Piggott, N. V. Sapra, J. Petykiewicz, and J. Vučković, *ACS Photonics* **5**, 301 (2018).

[5] P. Thureja, G. K. Shirmanesh, K. T. Fountaine, R. Sokhyan, M. Grajower, and H. A. Atwater, *ACS Nano* **14**, 15042 (2020), pMID: 33125844.

[6] D. Vercruyse, N. V. Sapra, K. Y. Yang, and J. Vučković, *ACS Photonics* **8**, 3085 (2021), <https://doi.org/10.1021/acsphotonics.1c01119>.

[7] E. A. Karahan, Z. Liu, A. Gupta, Z. Shao, J. Zhou, U. Khankhoje, and K. Sengupta, *Nature Communications* **15**, 10734 (2024).

[8] M. Bae, C.-C. Pan, C. Kang, J. Bae, D. Park, S. Lee, C. Park, H. Ren, J. Rho, H. Chung, and S. Kim, *APL Photonics* **10**, 100901 (2025).

[9] N. Barré, R. Shivaraman, S. Moser, P. Salter, M. Schmidt, M. Booth, and A. Jesacher, *Advanced Photonics Nexus* **2**, 036006 (2023).

[10] F. Alpeggiani, K. Y. Bliokh, F. Nori, and L. Kuipers, *Phys. Rev. Lett.* **120**, 243605 (2018).

[11] K. Y. Bliokh, Y. S. Kivshar, and F. Nori, *Phys. Rev. Lett.* **113**, 033601 (2014).

[12] J. Martínez-Romeu, I. Diez, S. Golat, F. J. R.-F. no, and A. Martínez, *Photon. Res.* **12**, 431 (2024).

[13] K. Y. Bliokh, A. Y. Bekshaev, and F. Nori, *New Journal of Physics* **15**, 033026 (2015).

[14] E. C. I. Paterson, J. Bourhill, M. E. Tobar, and M. Goryachev, *Phys. Rev. A* **112**, 013530 (2025).

[15] J. F. Bourhill, E. C. I. Paterson, M. Goryachev, and M. E. Tobar, *Phys. Rev. D* **108**, 052014 (2023).

[16] E. C. I. Paterson, J. Bourhill, M. E. Tobar, and M. Goryachev, (2025), arXiv:2510.01217 [physics.optics].

[17] E. C. I. Paterson, M. E. Tobar, M. Goryachev, and J. Bourhill, arXiv e-prints , arXiv:2506.07320 (2025), arXiv:2506.07320 [physics.class-ph].

[18] Y. Tang and A. E. Cohen, *Science* **332**, 333 (2011).

[19] E. Hendry, T. Carpy, J. Johnston, M. Popland, R. V. Mikhaylovskiy, A. J. Lapthorn, S. M. Kelly, L. D. Barron, N. Gadegaard, and M. Kadodwala, *Nature Nanotechnology* **5**, 783 (2010).

[20] C. Multunas, A. Grieder, J. Xu, Y. Ping, and R. Sundararaman, *Phys. Rev. Mater.* **7**, 123801 (2023).

[21] P. Sikivie, *Rev. Mod. Phys.* **93**, 015004 (2021).

[22] L. A. Völker, K. Herb, E. Janitz, C. L. Degen, and J. M. Abendroth, *The Journal of Chemical Physics* **158**, 161103 (2023).

[23] S. V. Kutsaev, A. Krasnok, S. N. Romanenko, A. Y. Smirnov, K. Taletski, and V. P. Yakovlev, *Advanced*

Photonics Research **2**, 2000104 (2021).

[24] T. Ozawa, H. M. Price, A. Amo, N. Goldman, M. Hafezi, L. Lu, M. C. Rechtsman, D. Schuster, J. Simon, O. Zilbermanberg, and I. Carusotto, Rev. Mod. Phys. **91**, 015006 (2019).

[25] W. Ma, Z. Liu, Z. A. Kudyshev, A. Boltasseva, W. Cai, and Y. Liu, Nature Photonics **15**, 77 (2021).

[26] B. Duan, B. Wu, J.-h. Chen, H. Chen, and D.-Q. Yang, Frontiers in Materials **8**, 791296 (2022).

[27] J. Gopalakrishnan and M. Neunteufel, “Guided modes of helical waveguides,” (2025), arXiv:2506.03276 [physics.optics].

[28] A. Taguchi, Y. Fukui, and K. Sasaki, Phys. Rev. Appl. **23**, L021002 (2025).

[29] COMSOL Inc., “COMSOL Multiphysics®,” (2024).

[30] J. Hennig, A. Maeder, AnnikaSchultheiss, and J. Feder, “Mph-py/mph: 1.3.0,” (2025).

[31] Z. Chaghazardi and R. Wüthrich, Journal of the Electrochemical Society **169**, 043510 (2022).

[32] M. H. Nasab, D. Gastaldi, N. F. Lecis, and M. Vedani, Additive Manufacturing **24**, 373 (2018).

[33] H. K. Rafi, N. V. Karthik, H. Gong, T. L. Starr, and B. E. Stucker, Journal of Materials Engineering and Performance **22**, 3872 (2013).

[34] J. Vaithilingam, R. D. Goodridge, R. J. Hague, S. D. Christie, and S. Edmondson, Journal of Materials Processing Technology **232**, 1 (2016).

[35] G. Strano, L. Hao, R. M. Everson, and K. E. Evans, Journal of Materials Processing Technology **213**, 589 (2013).

[36] M. Melia, J. Duran, J. Koepke, D. Saiz, B. Jared, and E. Schindelholz, npj Materials Degradation **4** (2020), 10.1038/s41529-020-00126-5.

[37] E. C. Santos, K. Osakada, M. Shiomi, Y. Kitamura, and F. Abe, Proceedings of the Institution of Mechanical Engineers, Part C: Journal of Mechanical Engineering Science **218**, 711 (2004), <https://doi.org/10.1243/0954406041319545>.

[38] S. Leuders, M. Thöne, A. Riemer, T. Niendorf, T. Tröster, H. Richard, and H. Maier, International Journal of Fatigue **48**, 300 (2013).

[39] C. Örnek, Corrosion Engineering, Science and Technology **53**, 531 (2018).

[40] Y.-C. Wu, C.-N. Kuo, Y.-C. Chung, C.-H. Ng, and J. C. Huang, Materials **12** (2019).

[41] P. Tyagi, T. Goulet, D. Brent, K. Klein, and F. Garcia-  
Moreno, in *IMECE2018* (American Society of Mechanical Engineers (ASME), Pittsburgh, PA, USA, 2018) pp. 2–5.

[42] U. S. Kim and J. W. Park, International Journal of Precision Engineering and Manufacturing-Green Technology **6**, 11 (2019).

[43] D. Landolt, Electrochimica Acta **32**, 1 (1987).

[44] N. P. Aryan, H. Kaim, and A. Rothermel, “Primary current distribution and electrode geometry,” in *Stimulation and Recording Electrodes for Neural Prostheses* (Springer International Publishing, Cham, 2015) pp. 25–30.

[45] T. Pérez, C. Ponce de León, F. C. Walsh, and J. L. Nava, Electrochimica Acta **154**, 352 (2015).

[46] P. Tyagi, T. Goulet, C. Riso, R. Stephenson, N. Chuenprateep, J. Schlitzer, C. Benton, and F. Garcia-Moreno, Additive Manufacturing **25**, 32 (2019).

[47] *Dimensional Characterizations Using SEM and Surface Improvement With Electrochemical Polishing of Additively Manufactured Microchannels*, Turbo Expo, Vol. Volume 8: Industrial and Cogeneration; Manufacturing Materials and Metallurgy; Marine; Microturbines, Turbochargers, and Small Turbomachines (2020) <https://asmedigitalcollection.asme.org/GT/proceedings-pdf/GT2020/84195/V008T18A007/6616359/v008t18a007-gt2020-14842.pdf>.

[48] S. Habibzadeh, L. Li, D. Shum-Tim, E. C. Davis, and S. Omanovic, Corrosion Science **87**, 89 (2014).

[49] C. Men, H. Li, and H. Zhang, Advanced Materials Research **233-235**, 985 (2011).

[50] D. L. Creedon, M. Goryachev, N. Kostylev, T. B. Sercombe, and M. E. Tobar, Applied Physics Letters **109**, 032601 (2016).

[51] R. Marzban, A. Adibi, and R. Pestourie, “Inverse design in nanophotonics via representation learning,” (2025), arXiv:2507.00546 [physics.app-ph].

[52] A. F. Gad, Multimedia Tools and Applications **1** (2023).

[53] F. Pedregosa, G. Varoquaux, A. Gramfort, V. Michel, B. Thirion, O. Grisel, M. Blondel, P. Prettenhofer, R. Weiss, V. Dubourg, J. Vanderplas, A. Passos, D. Cournapeau, M. Brucher, M. Perrot, and E. Duchesnay, Journal of Machine Learning Research **12**, 2825 (2011).

[54] J. Krupka, M. E. Tobar, J. G. Hartnett, D. Cros, and J.-M. L. Floch, IEEE Transactions on Microwave Theory and Techniques **53**, 702 (2005).